

Estimation of Ice Sheet Motion Using Satellite Radar Interferometry

Ian Joughin

Jet Propulsion Laboratory, 4800 Oak Grove Drive, Pasadena, CA 91109, USA.

Ron Kwok

Jet Propulsion Laboratory, 4800 Oak Grove Drive, Pasadena, CA 91109, USA.

Mark Fahnestock

JGESS, Dept. of Meteorology, University of Maryland at College Park, College Park, MD 20742.

ABSTRACT Satellite radar interferometry provides glaciologists with an important new tool for determining the motion and topography of large ice sheets. We examine the sources of error in interferometrically-derived ice-motion measurements, including those errors due to inaccurate estimates of the interferometric baseline. Several simulations are used to assess baseline accuracy in terms of tie-point error and the number and distribution of tie points. These results give insight into how best to select tie points and also demonstrate the level of accuracy that can be achieved. Examination of two representative cases likely to occur in mapping ice-sheet motion leads to the conclusion that with adequate tie-point information ice velocity can be measured with an accuracy of a few m/yr. A method to correct horizontal velocity estimates for the effect of vertical displacement using surface slopes is also developed. Finally, we estimate the single-component velocity field for an area on the Humboldt Glacier in northern Greenland using interferograms formed from ERS-1 SAR images. We estimate that these velocity measurements are accurate to within 2.3 m/yr.

INTRODUCTION

Knowledge of ice-flow velocity and strain rate is important in assessing an ice sheet's mass balance and in understanding its flow dynamics. Ground-based measurements of ice-sheet velocities are scarce because of logistical and technical difficulties. Ice-flow velocities have

been measured from the displacement of features observed in pairs of visible (Scambos and others, 1992; Ferrigno and others, 1993) or synthetic aperture radar (SAR) images (Fahnestock and others, 1993), but these methods do not work well for the large, featureless areas that comprise much of the ice sheets.

Several recent papers have indicated that satellite radar interferometry (SRI) provides a potential means to measure ice-flow velocity. Using SRI, Goldstein and others (1993) estimated velocities for an area on the Rutford Ice Stream, Antarctica. Interferograms of the Hemmen Ice Rise on the Filchner-Ronne Ice Shelf have been studied by Bartl and others (1994). Joughin and others (1995a) have examined interferograms from a 400-km-long area on the Greenland ice sheet that exhibit complex phase patterns due to motion. Agreement between interferometric and *in situ* measurements of velocity was obtained by Rignot and Jezek (1995). Kwok and Fahnestock (1996) have measured relative velocity on an ice stream in Greenland.

While these papers have demonstrated the great potential of SRI for measuring ice-sheet motion, the data in these studies are subject to error due to difficulty in estimating the interferometric baseline. Estimates of the baseline determined from satellite ephemeris data that is derived from satellite tracking and orbital modelling are typically accurate to within a few meters (Solaas and Coulson, 1994). While adequate for many purposes, this level of accuracy can introduce substantial error in motion estimates. For example, a 1 meter baseline error introduces a phase ramp of about 4 fringes across a 3-day interferogram, yielding a relative velocity error of 39 m/yr across a 100-km wide image. Tie points (points of known elevation and velocity) can be used to improve the accuracy of baseline estimates (Zebker and others, 1994). Because estimates of baselines from orbital data alone are unlikely to yield reasonable accuracy, wide-scale map-

ping of ice-sheet velocities requires a combination of interferometric data and tie points determined from field-based global positioning system (GPS) surveys. The cost of measuring such tie points is high. Thus, it is important to understand how to select tie points to achieve maximum accuracy at minimum cost.

We begin with a brief introduction to interferometric principles and techniques. The next section describes an error model for SRI velocity estimation. The results of simulations are then examined to determine how baseline accuracy is affected by various factors. Velocity errors are examined for two typical situations that are likely to occur in measuring ice-sheet motion. Next a method is developed to improve estimation of horizontal velocity by compensating for the effect of vertical motion using interferometrically-derived estimates of the surface topography. We then apply this technique to estimate the single-component velocity field for an area on the Humboldt Glacier, Greenland. Our results confirm that SRI provides an important new means for measuring ice velocity, as indicated by earlier studies, and that a small number of field-determined motion and elevation tie points will allow production of calibrated maps of ice-flow speed covering thousands of square kilometers.

INTERFEROMETRY BACKGROUND

The **geometry** of an interferometric SAR is shown in Figure 1. The interferometer acquires two images of the same scene with SARs located at S_1 and S_2 . The first SAR is at altitude h . From S_1 , the range, r_0 , and look angle, θ , to a point on the surface is determined by the ground range, y , and elevation, z , above some reference ellipsoid. The range to the same point from the SAR at S_2 differs from r_0 by Δ . For a single-pass system, such as TOPSAR (Zebker and others,

where k is the wave number and W_1 is a complex, circular Gaussian random variable (RV) with amplitude A , and phase ϕ_1 (Rodriguez and Martin, 1992). The modulo -2π phase from a single complex image cannot be used to determine range since it has a uniform probability distribution Over $[0, 2\pi)$. A complex interferogram is formed as the product of one complex SAR image with the complex conjugate of a second. The phase of this product is given by

$$\angle V_1 V_2^* = (2k\Delta + (\phi_1 - \phi_2)) \bmod(2\pi) \quad (2)$$

Although ϕ_1 and ϕ_2 are both uniformly distributed, if W_1 and W_2 are correlated, their difference, $(\phi_1 - \phi_2)$, is not uniformly distributed. In fact, the distribution of the phase difference can be quite sharply peaked if the complex images are well correlated.

Even with a narrow phase distribution, the phase difference is still only known modulo 2π . A phase-unwrapping algorithm (Goldstein and others, 1988) is used to remove the 2π ambiguity. With repeat-pass interferometry, the range difference between passes is determined using

$$\hat{\Delta} = \frac{\phi_{unwrap}}{2k} = \frac{\lambda}{4\pi} \phi_{unwrap} \quad (3)$$

Where ϕ_{unwrap} denotes the unwrapped interferometric-phase difference and λ is the radar wavelength. Error in this estimate is introduced by (ϕ_1, ϕ_2) . Note that phase unwrapping algorithms usually yield the relative phase as there is an unknown constant of integration associated with the unwrapped solution. It is assumed here that ϕ_{unwrap} has been processed to remove this ambiguity (i.e., with the aid of tie points). The ERS-1 SAR operates at a wavelength of $\lambda = 5.656$ cm so that Δ typically can be measured with sub-centimeter accuracy.

With a repeat-pass interferometer, Δ is affected by both topography and any movement of the surface that is directed toward or away from the look direction of the radar between orbits. The interferometric phase can therefore be expressed as the sum of displacement- and topography-dependent terms,

$$\phi_{unwrap} = \phi_{topography} + \phi_{displacement} \quad (4)$$

Motion

The contribution to the overall phase from surface displacement is given by

$$\phi_{displacement} = 2k (\Delta_{d,y} \sin \psi - \Delta_{d,z} \cos \psi) , \quad (5)$$

where $\Delta_{[1,y]}$ denotes the component of the range difference tangential to the surface of a reference ellipsoid that is directed across track, and $\Delta_{d,z}$ denotes the component normal to the ellipsoid. The incidence angle, ψ , is defined with respect to the local normal to the ellipsoid (see Figure 1). When the surface velocity does not change over the period, δT , between acquisition of images, the phase due to motion is

$$\phi_{displacement} = 2k \delta T (v_y \sin \psi - v_z \cos \psi) . \quad (6)$$

Topography

Referring to Figure 1, baseline is related to the range difference due to topography by

$$B_n \sin \theta_d + B_p \cos \theta_d = \Delta_{topography} - \frac{\Delta_{topography}^2}{2r_0} + \frac{B^2}{2r_0} . \quad (7)$$

ignoring the $\Lambda_{topography}^2$ term in (7) we can approximate the range difference by

$$\Lambda_{topography} \approx -11.7 \sin \theta_d - B_p \cos \theta_d + \frac{B^2}{2r_0}. \quad (8)$$

The deviation of the look angle from the center look angle, θ_d , is related to range and surface elevation by

$$\theta_d = \theta - \theta_c = \arccos \left(\frac{r_0^2 + 2R_e(H-z) + H^2 - r^2}{2(R_e + H)r_0} \right), \quad (9)$$

where R_e denotes the radius of the earth. Once $\Lambda_{topography}$ is determined from the phase, equations (7) and (8) are solved to determine the height and groundrange of each point in the image (Jand Goldstein, 1990).

There is a nearly linear phase variation from the uniform change in groundrange, y , across an image, which is much greater in magnitude than the phase variation due to topography. It is often useful to remove the ground-range variation by subtracting the phase ramp corresponding to a zero-height surface, ϕ_{flat} . The effect of elevation on the interferometric phase can then be approximated as

$$\phi_z = \phi_{topography} + \phi_{flat} - \frac{2kB_n}{\sin \theta_c} z \quad (10)$$

This approximation, which is not valid for computing elevations, indicates that the sensitivity of an interferometer to topography is proportional to B_n . But, when we refer to the baseline length below, we mean the length of B_n , rather than the actual baseline length, B .

Baseline Estimation

IRS-1 orbits are not known well enough to estimate baselines with the level of accuracy

needed to generate DIMs and estimate motion. As a result, the baseline must be determined using tie points (Zebker and others, 1994). The baseline varies along the satellite track. Over the length of an ERS-1 interferogram, we model baseline variation as a linear function of the along-track coordinate, x . The normal component of baseline is then represented as

$$B_n = B_n^c + \delta B_n \left(\frac{x - x_c}{L_x} \right), \quad (11)$$

where B_n^c is the normal component of baseline at the frame center, x_c , and δB_n is the change in B_n over the length of the frame, L_x . Similarly, the parallel component of baseline can be modeled as

$$B_p = B_p^c + \delta B_p \left(\frac{x - x_c}{L_x} \right). \quad (12)$$

With a linear model for baseline variation, there are four unknown parameters: $B_n^c, B_p^c, \delta B_n, \delta B_p$. There is also an unknown constant associated with the phase after it has been unwrapped. An approximation can be made to implicitly incorporate this constant into the baseline solution so that only the four baseline parameters need to be determined (Joughin, 1995). The expression given by (7) is nonlinear with respect to these parameters. The problem is easily linearized by replacing the nonlinear terms, which are small, with estimates of their values obtained from satellite ephemeris data. The baseline parameters then are determined using a standard linear least-squares algorithm (Press and others, 1992) with at least four tie points.

MOTION ESTIMATION ERROR

Error Model

The effect of topography must be removed from an interferogram before velocity estimates can be made. With a nearly-zero baseline, the effect of Topography is negligible and can be ignored (Goldstein and others, 1993). For longer baselines an independent digital elevation model (DEM) can be used to estimate and remove $\phi_{topography}$ (Massonnet and others, 1993). An alternative method is to cancel $\phi_{topography}$ using an appropriately scaled topography-only interferogram (Gabriel and others, 1991). In this paper we use interferometrically-derived DEMs to remove topographic phase variation,

Interferograms are subject to random phase error due to speckle, σ_ϕ . If the effect of vertical velocity is ignored, then applying (6), the velocity error due to phase noise is

$$\sigma_{e_\phi, v_y} = \frac{1}{2k\delta T \sin \psi} \sigma_\phi. \quad (13)$$

Estimates of $\phi_{displacement}$ are affected by inaccuracy in the DEM used to estimate $\phi_{topography}$. Using (10), the standard deviation of this error is expressed as

$$\sigma_{e_z} = \frac{2kB_n}{\sin \theta_c r_0} \sigma_z, \quad (14)$$

where σ_z denotes the standard deviation of the DEM error. Since this error is proportional to baseline length, its effect is negligible for sufficiently small baselines (Goldstein and others, 1993). If we ignore the v_z term in (6), then the error in the velocity estimate is given by

$$\sigma_{e_z, v_y} = \frac{B_n}{\delta T r_0 \sin \theta_c \sin \psi} \sigma_z. \quad (15)$$

For typical ERS-1 parameters this error is equal to $0.00106 B_n \sigma_z$ m/yr for a 3-day interferogram.

A 50-m baseline and a DEM error of **50 m then** would yield a velocity error of **2.65** m/yr.

In canceling the topography the baseline-dependent phase ramp due to groundrange is also removed (i.e., ϕ_{flat}). Thus, inaccurate baselines lead to error through the imperfect cancellation of this elevation-independent phase variation. If the estimated baseline components are \hat{B}_n and \hat{B}_p , then applying (8) and neglecting small nonlinear terms, the resulting phase error is

$$\phi_{e_B} = -2k [(B_n - \hat{B}_n) \sin \theta_{d,flat} + (B_p - \hat{B}_p) \cos \theta_{d,flat}] \quad (16)$$

The variance of this error is

$$\sigma_{e_B}^2 = 4k^2 \left[\left(\sigma_{\hat{B}_n} \sin \theta_{d,flat} \right)^2 + \left(\sigma_{\hat{B}_p} \cos \theta_{d,flat} \right)^2 + 2 \sin \theta_{d,flat} \cos \theta_{d,flat} C_{\hat{B}_n \hat{B}_p} \right], \quad (17)$$

where $C_{\hat{B}_n \hat{B}_p}$ denotes the covariance of \hat{B}_n and \hat{B}_p . If we ignore the vertical component of velocity in (6), the variance of the error in v_y due to baseline inaccuracy is

$$\sigma_{e_{B v_y}}^2 = \left(\frac{1}{\delta T \sin \psi} \right)^2 \left[\left(\sigma_{\hat{B}_n} \sin \theta_{d,flat} \right)^2 + \left(\sigma_{\hat{B}_p} \cos \theta_{d,flat} \right)^2 + 2 \sin \theta_{d,flat} \cos \theta_{d,flat} C_{\hat{B}_n \hat{B}_p} \right]. \quad (18)$$

This is often the largest source of error in interferometric estimates of ice velocity.

Applying (11), the variance in estimate of the linearly varying baseline can be expressed as

$$\sigma_{\hat{B}_n}^2 = \sigma_{\hat{B}_n^c}^2 + \sigma_{\delta \hat{B}_n}^2 \left(\frac{x - x_c}{L_x} \right)^2 + 2 C_{\hat{B}_n^c \delta \hat{B}_n} \left(\frac{x - x_c}{L_x} \right). \quad (19)$$

We may also write a similar expression for $\sigma_{\hat{B}_p}^2$. The covariance between baseline components is given by

$$C_{\hat{B}_n \hat{B}_p} = C_{\hat{B}_n^c \hat{B}_p^c} + \left(C_{\delta \hat{B}_n \hat{B}_p^c} + C_{\hat{B}_n^c \delta \hat{B}_p} \right) \left(\frac{x - x_c}{L_x} \right) + C_{\delta \hat{B}_n \delta \hat{B}_p} \left(\frac{x - x_c}{L_x} \right)^2 \quad (20)$$

These expressions are used in (18) to determine velocity error due to baseline inaccuracy.

The error at any given point in the estimated velocity field is a random variable, since it is a function of the random baseline error. For a given baseline estimate, however, the error for the entire image is a 2-dimensional function described by four parameters. As a result, the velocity error has a high degree of spatial correlation. For example, because $\sin \theta_d$ changes sign at the image center, velocity errors usually change sign from one side of the image to the other. For a given point along track, x , the relative error from θ_d to $-\theta_d$ is approximately twice the absolute error at each of these points. This should be kept in mind when interpreting results computed using (18).

Accuracy of Baseline Estimates

In this section we examine the accuracy of baseline estimates using synthetic interferograms. Because it is often difficult to obtain tie points, it is important to understand how their number, accuracy, and distribution affects baseline accuracy and, thus, the accuracy of velocity estimates. With this knowledge optimal tie-pointing strategies can be devised to minimize field effort.

For the simulations we used a 303.2-km-long by 100-km-wide DEM of typical ice-sheet and bedrock (ice free) topography. From the DEM we generated synthetic interferograms for several baseline lengths. All of the tie points are assumed to be stationary (i.e., located on bedrock). Non-stationary tie points (i.e., points on the ice sheet) are examined in the next section. Noise was added to the tie points and to the interferogram. Baselines were estimated using a least-squares algorithm (Press and others, 1992; Joughin, 1995). For each simulation, statistics were evaluated for the baseline estimates from 250 realizations. Because several parameters con-

tribute to baseline accuracy, there is no way to illustrate baseline accuracy for all possible sets of parameters here. In each of the simulations a single parameter is varied while the others are held fixed. The results will change when the other parameters are no longer fixed, although the trends should be similar.

The first simulation was performed to determine the effect of baseline length on estimation accuracy. For several baseline lengths we computed estimates for Gaussian phase noise of $\sigma_\phi = 0$ rad and $\sigma_\phi = \frac{\pi}{3}$ rad and Gaussian tie point error of $\sigma_T = 20$ m. One hundred tie points ($N_{ties} = 100$), evenly spaced over an area $D_y = 86.9$ km wide by $D_x = 85.8$ km long, were used. Standard deviations of the estimated parameters are shown in Figure 2.

With no phase noise baseline error increases linearly with B_n . This increase occurs because an interferometer with a shorter baseline is less sensitive to topography so that the effect of tie-point error is smaller. When there is phase noise, estimation accuracy improves with decreasing baseline length until a point where there is little further improvement. This point occurs where the effect of phase noise on baseline accuracy, which is independent of baseline length, becomes larger than that of tie-point error. Thus, the amount of improvement that can be gained by using a shorter baseline is limited by the amount of phase noise relative to the amount of elevation tie-point error.

Baseline estimates can be improved by using more than the minimum of four tie points in the least-squares solution (Zebker and others, 1994). Figure 3 illustrates the standard deviation of the estimates of \hat{B}_n^c and $\delta\hat{B}_n$ as a function of the number of tie points, N_{ties} . The tie points are arranged on a regular grid $D_y = 86.9$ km by $D_x = 85.8$ km. Each time N_{ties} is increased, the spacing between points is decreased so that area covered by the tie points remains unchanged.

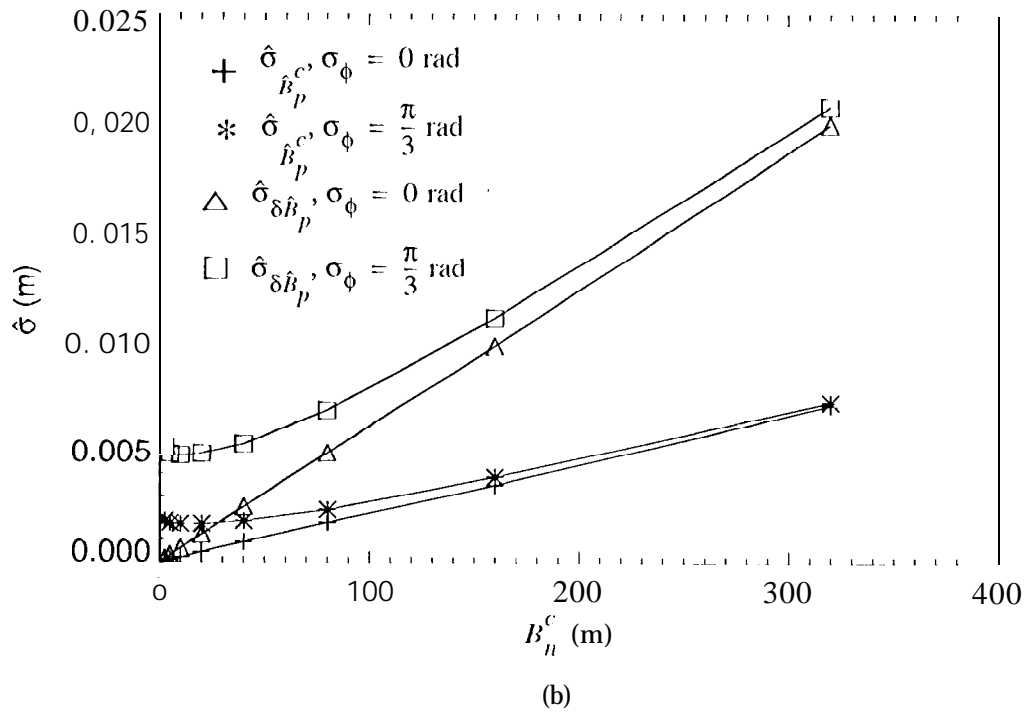
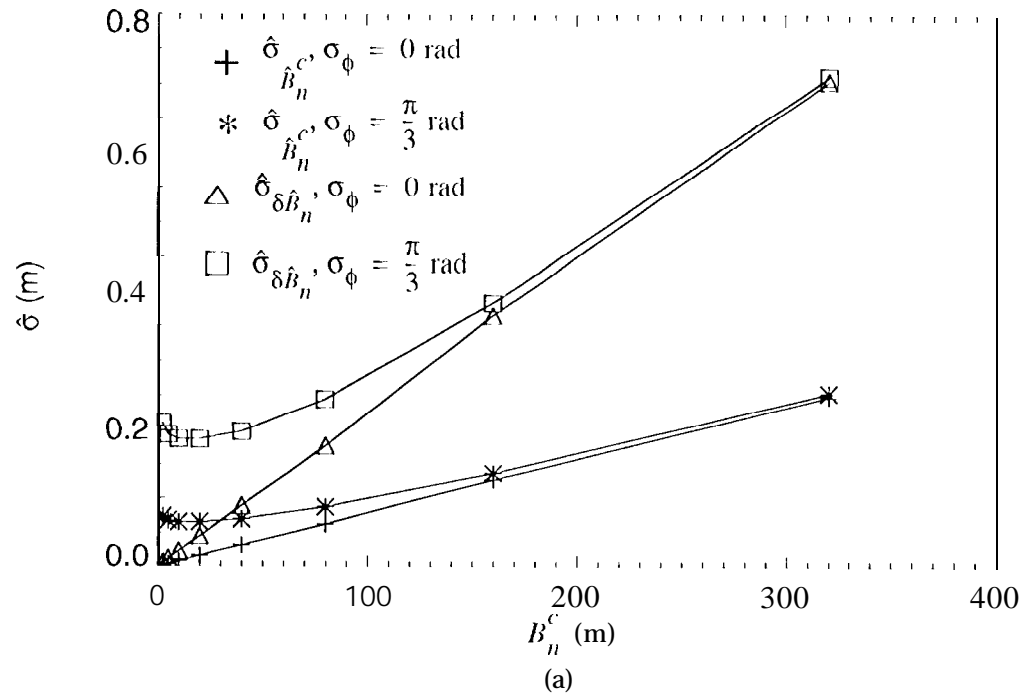


Figure 2. Standard deviations of (a) \hat{B}_n^c , $\delta\hat{B}_n$, (b) \hat{B}_p^c , and $\delta\hat{B}_p$ for 250 estimates as a function of B_n^c . Estimates were made for $N_{lies} = 100$, $\sigma_z = 20 \text{ m}$, $\delta B_n = ()$, $B_p^c = 25 \text{ m}$, $\delta B_p = ()$, $D_y = 86.9 \text{ km}$, $D_x = 85.8 \text{ km}$, and $L_x = 303.2 \text{ (km)}$.

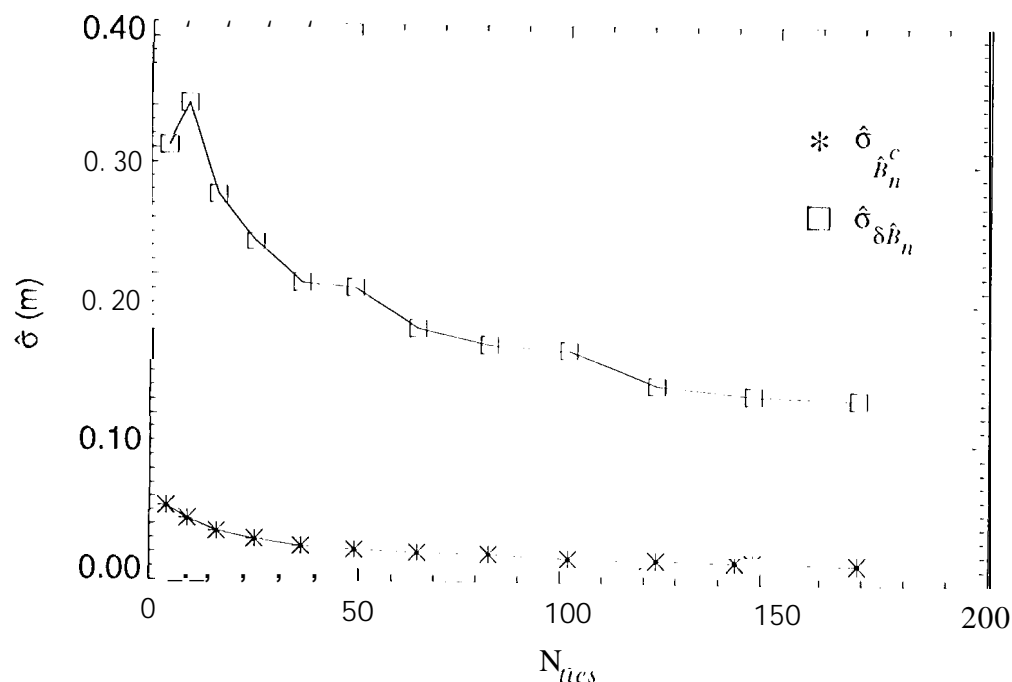


Figure 3. Standard deviations of \hat{B}_n^c and $\delta\hat{B}_n$ for 250 estimates as a function of the number of tie points, N_{ties} , for $B_n^c = 10111$, $\delta B_n = 0$, $B_p^c = 25111$, $\delta B_p = ()$, $D_y = 86.9$ km, $D_x = 85.8$ km, $L_x = 303.2$ km, $\sigma_\phi = \frac{\pi}{3}$ rad, and $\sigma_z = 20$ m.

The squared error for the fits (not shown) falls off as $\frac{1}{N_{ties}}$. In general, the standard deviations of the parameter estimates, including those not shown in Figure 3, decrease as $\frac{1}{\sqrt{N_{ties}}}$. An exception is seen in Figure 3, where $\hat{\sigma}_{\delta B_n}$ increases when N_{ties} increases from 4 to 9. The squared error for the overall fit, however, still decreases as expected.

For a fixed number of tie points, the distance between points affects the accuracy of baseline estimates. To examine this dependence, we used 4 tie points arranged to form a rectangle (D_y by D_x) with sides parallel to those of the swath. Figure 4 shows the results plotted as a function of the product, $(D_y \times D_x)$. Each time D_x and D_y were increased, they were scaled by the same factor

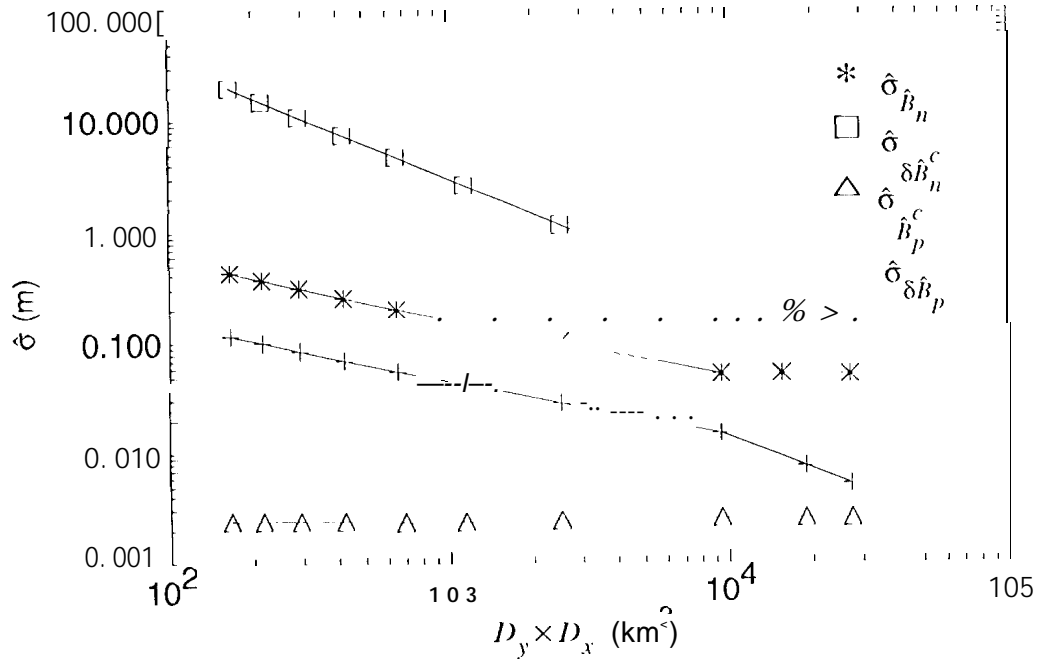


Figure 4. Standard deviations from 250 estimates of the baseline parameters as a function of area covered by 4 tie points. Results are for $B_n^c = 10$ m, $\delta B_n = 0$ m, $B_p^c = 25$ m, $\delta B_p = 0$ m, $L_x = 303.2$ km, $\sigma_\phi = \frac{\pi}{3}$ rad, and $\sigma_z = 20$ m.

with the exception of the last two points where only D_x was Scaled because D_y could not be scaled further without exceeding the swath width. The primary effect of B_p^c on the interferometric phase is to determine a constant bias so that the estimate of this parameter is insensitive to tie-point spacing, as can be seen from the results in Figure 4. Error in the estimate of a derivative is inversely proportional to the distance between points. Consequently, the error in the estimate $\delta \hat{B}_p$ decreases as $\frac{1}{D_x}$, as illustrated in Figure 4. Likewise, $\hat{\sigma}_{\hat{B}_n}$ is inversely proportional to D_y since B_n determines the slope of the phase ramp across an interferogram. Finally, δB_n determines variation of the baseline with respect to x and also affects the slope of the phase ramp so

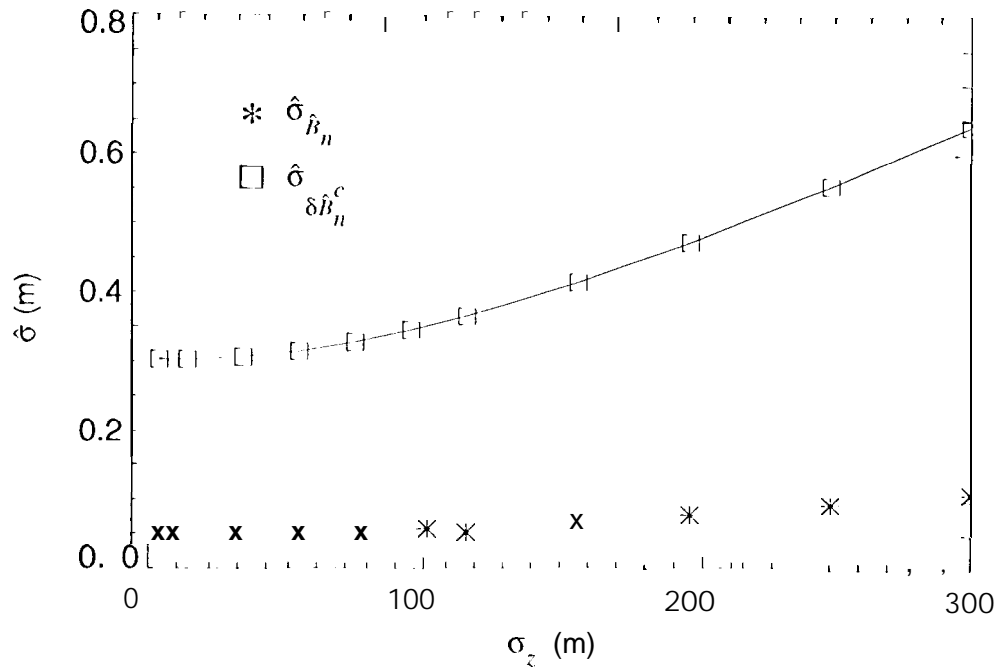


Figure 5. Standard deviations \hat{B}_n^c and $\delta \hat{B}_n$ for 250 estimates as a function of tie-point noise, σ_z , for $B_n^c = 10$ m, $\delta B_n = 0.11$, $B_p^c = 25111$, $\delta B_p = 0$ m, $D_y = 86.9$ km, $D_x = 85.8$ km, $\sigma_\phi = \frac{\pi}{3}$ rad, and $L_x = 303.2$ km.

that error in its estimate is inversely proportional to $D_y \times D_x$. Because increasing tie point spacing affects the errors for each of the estimates differently, it is difficult to say exactly how the quality of the overall fit improves. It is clear, however, that increasing the distance between tie points significantly reduces error. A specific example is given in the next section.

Error in the baseline estimates is caused by phase and tie-point noise. Figure 5 shows baseline error as a function of tie-point error for a fixed level of phase error. Baseline error improves almost linearly with decreasing tie-point error until a point where phase error begins to dominate and there is little significant improvement. At this point phase noise must be reduced to realize

Tic-Point Type	Number of Tic Points	B_n (m)	D_y (km)	D_x (km)	σ_z (111)	σ_ϕ (rad)
bedrock	100"	10	50	50	100"	$\frac{\pi}{20}$
ice Sheet	4	10	50	50	1	$\frac{\pi}{4}$

Table 1. Parameters for simulations with ice-sheet and bedrock tie points

further improvement.

Velocity Error

in this section we examine the velocity error due to baseline inaccuracy for two typical situations that are likely to arise in the interferometric estimation of ice velocity. in the first case we consider baselines estimated using stationary tic points on areas of bedrock near the ice-sheet margin. in this case it is important to understand how far onto the ice sheet the baseline estimate can be extended while maintaining reasonable accuracy for the velocity estimate. in the second case baselines are determined using non-stationary tic points from areas on the ice sheet where there is little or no exposed bedrock to provide stationary points. In this situation it is important to understand how to select tic points to achieve sufficiently accurate velocity estimates with minimum field effort.

We begin using simulated bedrock tic points for a typical set of constraints. The parameters for the simulation are listed in Table 1, DEMs available for areas near ice-sheet margins typically have low horizontal and vertical resolution. Error in locating tic points in areas of an image where there are steep slopes increases the effective tic-point error. For these reasons we assume a

relatively large tie-point error of $\sigma_z = 100$ m. Since it is easy to obtain a large number of tie points from a DIM, we use 100 tie points distributed uniformly over a 50-km-by-50-km area. With sufficient averaging, phase noise can be kept small. For the simulation we use $\sigma_\phi = \frac{\pi}{20}$.

The sample variance and covariance of 250 baseline estimates determined from bedrock tie points are given in Table 2. A contour plot of σ_{e_B, v_y} is given in Figure 6(a). Since we are interested in using bedrock areas at the ice margin, the tie points are centered at $x - x_c = 125$ km, with the edge of the ice sheet at $x - x_c = -100$ km. Although the baselines were estimated for $L_x = 303.2$ km, there is no reason velocity error cannot be computed for $|x - x_c| > L_x$. In this figure the error is plotted out to a distance of 500 km inland from the ice-sheet margin ($x - x_c = 400$ km).

From Figure 6(a) we see that velocity error is smallest in the area near the tie points and becomes steadily worse with increasing distance inland. Looking at the variation across the image, we see that accuracy is best at the center and worst toward the edges. At 200 km ($x - x_c = 400$ km) inland the absolute error is less than 5 m/yr with a relative error across the image of approximately 8 m/yr. The absolute error at 500 km from the ice sheet margin is just over 11 m/yr, and the relative error is about 17 m/yr, which for many applications is unacceptably large.

Bedrock area is limited and in many cases smaller than in this example. "But, increasing the bedrock area from which tie points are chosen is often not an option. Because it is quite small to begin with, reduction of phase noise will achieve little improvement. The baseline is short so that there is little to be gained by using an even smaller baseline. Minor improvement might be achieved by increasing the number of tie points, but only so long as the tie-point errors remain

Tic-Point Type	Bedrock Tie Points	Ice-Sheet Tie Points
$\hat{\sigma}_{\hat{B}_n^c} \text{ (m}^2\text{)}$	0.0252	0.005660
$\hat{\sigma}_{\hat{B}_p^c} \text{ (m}^2\text{)}$	6.5e-6	3.25e-6
$\hat{\sigma}_{\delta \hat{B}_n} \text{ (m}^2\text{)}$	0.43	0.791
$\hat{\sigma}_{\delta \hat{B}_p} \text{ (m}^2\text{)}$	3.55e-5	-4.73e-4
$\hat{C}_{\hat{B}_n^c \hat{B}_p^c} \text{ (m}^2\text{)}$	-1.23e-4	-3.87e-5
$\hat{C}_{\delta \hat{B}_n \delta \hat{B}_p} \text{ (m}^2\text{)}$	-6.80e-4	-0.00593
$\hat{C}_{\hat{B}_n^c \delta \hat{B}_p} \text{ (m}^2\text{)}$	-2.85e-4	-1.64e-4
$\hat{C}_{\delta \hat{B}_n \hat{B}_p^c} \text{ (m}^2\text{)}$	-2.90e-4	-9.91e-5

Table 2. Moments of baseline estimates from simulations with ice-sheet and bedrock tie points.

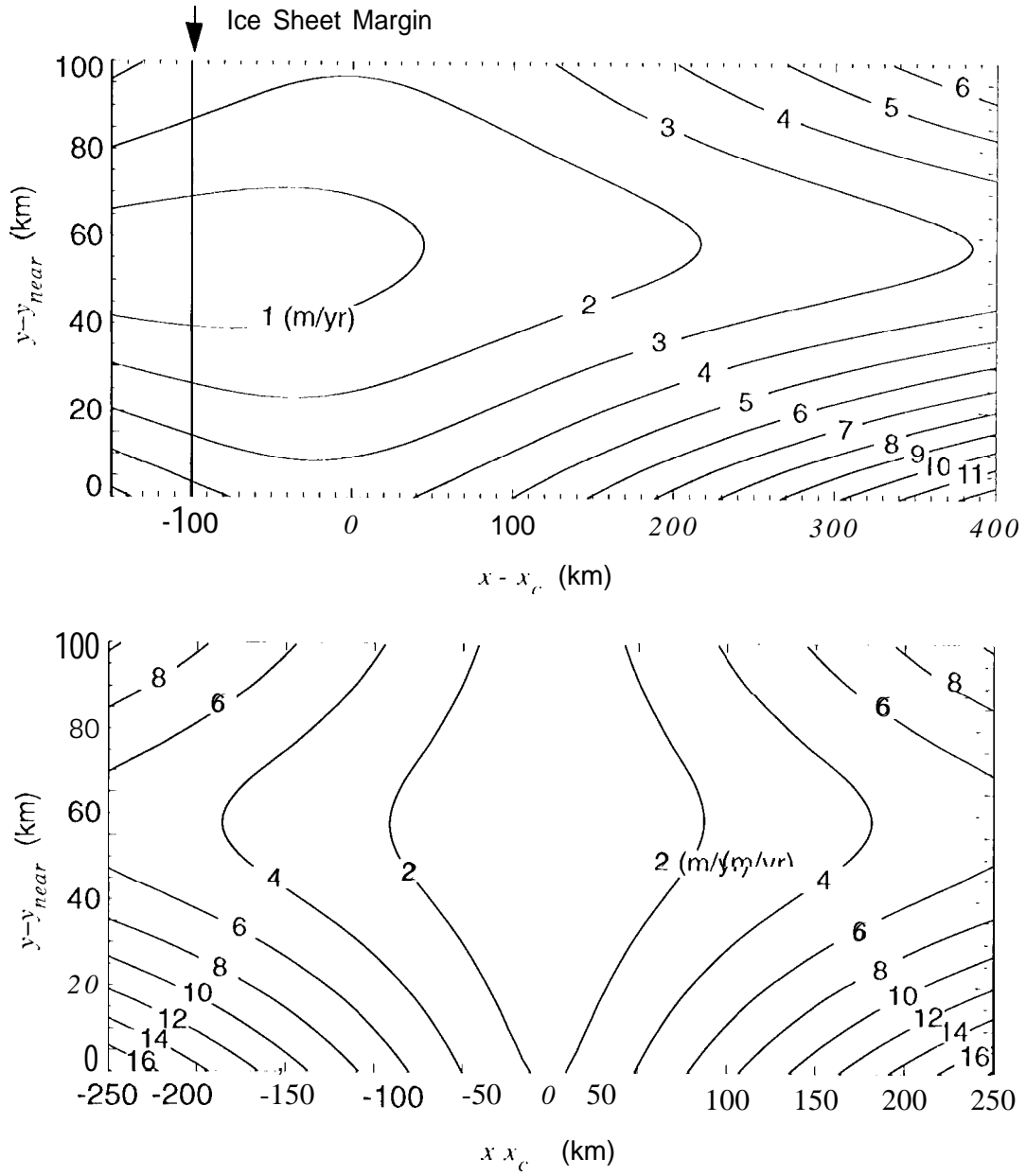


Figure 6. Velocity error, $\sigma_{e_{B^*v_y}}$, for simulated (a) bedrock and (b) ice-sheet tie points for a 3-day interferogram. Simulation parameters are given in Table 1, and the statistics of the estimated baselines used to compute $\sigma_{e_{B^*v_y}}$ are included in Table 2.

uncorrelated. Because tie-point errors are large, the most significant improvement can be realized by decreasing tie-point error. For example, if tie-point error is reduced to 25 μm , then velocity error decreases by a factor of about 3. Lesser gains are realized by a further decrease in tie-point error because phase noise begins to dominate.

Next we examine the case where velocity tie points measured on the ice sheet are used. The parameters for a typical set of ice-sheet tie points are given in Table 1. Because it is difficult to make such measurements, the minimum of four tie points is assumed. If tie-point velocity is measured over the period of a few weeks using GPS receivers, the error should be small. A high estimate of the velocity tie-point error is 0.8 m/yr. This error is included in the simulation by modeling it as an equivalent phase error of $\sigma_\phi = \frac{\pi}{5}$ radians. An additional phase error of $\sigma_\phi = \frac{3\pi}{20}$ radians due to decorrelation yields a total phase error of $\sigma_\phi = \frac{\pi}{4}$ radians. Allowing for errors in locating the tie points within the SAR imagery, we assume, elevation error of $\sigma_z = 1$ m. The tie points are arranged to form a square with 50-km sides centered about x_c . The moments of the baseline estimates determined from this simulation are included in Table 2, and the corresponding velocity error is shown in Figure 6(b).

The baseline estimates for the ice-sheet tie points are not as accurate as those for bedrock tie points, causing the velocity error to be larger. Even though the elevation error is much smaller, baseline accuracy is reduced because fewer tie points are used. Since the elevation error is small, no real improvement can be gained by improving the elevation estimates. Increasing the number of tie points would help, but the additional field effort may outweigh the gain. Tie-point velocity error also contributes to the larger velocity errors. Since a large estimate of the tie-point velocity error was used, significant improvement is possible if tie-point velocities are measured more

accurately. If logistical constraints permit, increasing the separation of tic points will achieve much improved results. For example, if the distances between tic points are increased to $D_y = 100$ km and $D_x = 300$ km, the velocity error decreases by a factor of about 8 to yield a maximum absolute error of just over 2 m for the entire 100-km by 500-km area. Thus, for tic points on the ice sheet maximizing the spacing between points appears to be the best method for improving velocity estimates.

The results presented thus far have assumed a 3-day separation (i.e., $\delta T = 3$ days) for interferograms. Tic-point elevation error leads to error in the estimated velocity field. This error is inversely proportional to δT . In particular for bedrock tic points, it is often possible to improve velocity estimates by using a longer temporal baseline. This situation is more complicated for non-stationary tic points. Error that is the result of error in the tic-point velocity measurements is independent of δT so it does not decrease when δT is increased. "Thus, little is gained by using a longer temporal baseline if tic-point velocity error is the dominant source of baseline error.

Temporal decorrelation increases over time, placing an upper limit on δT . Temporal decorrelation is generally highest in regions with large strain rates. Therefore, longer temporal baselines are better suited for use in areas of slow moving ice.

It is important to note that the preceding analysis is based on the assumption that the baseline varies linearly along track. Although we have obtained good results applying this assumption over distances of a few hundred kilometers, nonlinear variation may have an effect over greater distances. If such variations occur, then more than four tic-points are required either to fit the baseline variation to a higher-order polynomial or to use a piece-wise linear approximation.

ESTIMATION OF THE ACROSS-TRACK VELOCITY FIELD

The displacement measured by an interferometric SAR is directed toward or away from the radar, but an estimate of the horizontal velocity is desired. Applying (6), the horizontal velocity is related to the phase clue to displacement by

$$v_y = -\frac{\phi_{displacement}}{2k\delta T \sin \psi} + v_z \cot \psi. \quad (21)$$

A simple approach to estimating horizontal velocity is to ignore the vertical-velocity term in the equation. Joughin and others (1995a) have shown that while vertical velocity is small in comparison with horizontal velocity, v_z is responsible for much of the phase variability over length scales of less than a few ice thicknesses. These fluctuations present little problem in determining the velocity field averaged over a few ice thicknesses. The error induced by neglecting vertical motion is far more significant, however, when examining "ice-flow-velocity" variation over lengths scales comparable to the ice thickness. In particular, estimates of the local strain rate are severely affected by velocity error due to uncompensated vertical motion. As a result, it is often necessary to correct for the effect of vertical velocity when estimating horizontal velocity.

If we assume surface parallel flow, then the vertical velocity is related to the horizontal velocity by

$$v_z = v_x \frac{\partial}{\partial x} z(x, y) + v_y \frac{\partial}{\partial y} z(x, y) \quad (22)$$

Substituting this expression into (21) yields,

$$v_y = -\frac{\phi_{displacement}}{2k\delta T \sin \psi} + \cot \psi \left(v_x \frac{\partial}{\partial x} z(x, y) + v_y \frac{\partial}{\partial y} z(x, y) \right), \quad (23)$$

which is solved to yield

$$v_y = \frac{\left(\frac{\phi_{displacement}}{2k\delta T \sin \psi} + v_x \cot \psi \frac{\partial}{\partial x} z(x, y) \right)}{\left(1 - \cot \psi \frac{\partial}{\partial y} z(x, y) \right)} \quad (24)$$

With this expression we now need the other horizontal velocity component, v_x , to determine v_y .

If we had another interferogram from a second look direction (i.e., an ascending pass), we could derive a similar expression relating v_y to v_x . With these two equations and (22), the three components of the velocity field can be determined. We discuss the case where there are no interferograms from a second look direction below.

VELOCITY FIELD FOR THE HUMBOLDT GLACIER

The Humboldt is an outlet glacier in northwestern Greenland that discharges into the Kane Basin. Figure 7 shows an ERS-1 SAR amplitude image of the lower part of the Humboldt. The location of the image is shown on the map in Figure 8. The darker areas on the ice sheet along the bright calving face are bare ice in the ablation area. The transition from this region to the adjacent brighter region marks the border of the wet-snow zone (Fahnestock and others, 1993). The brighter areas in the lower corners of the image are within the percolation zone. Several lakes are visible, which show up as small bright circular regions in this winter imagery.

We obtained SAR data from orbits 2904, 2947 and 2990, which spanned the interval from February 4 to February 10, 1992. The UK-PAF (United Kingdom Processing and Archiving Facility) SAR processor produces single-look, complex images that yield interferograms with low-frequency errors (Joughin and others, 1995b) and phase discontinuities. To circumvent this problem, we ordered raw SAR data and processed it ourselves to obtain single-look, complex

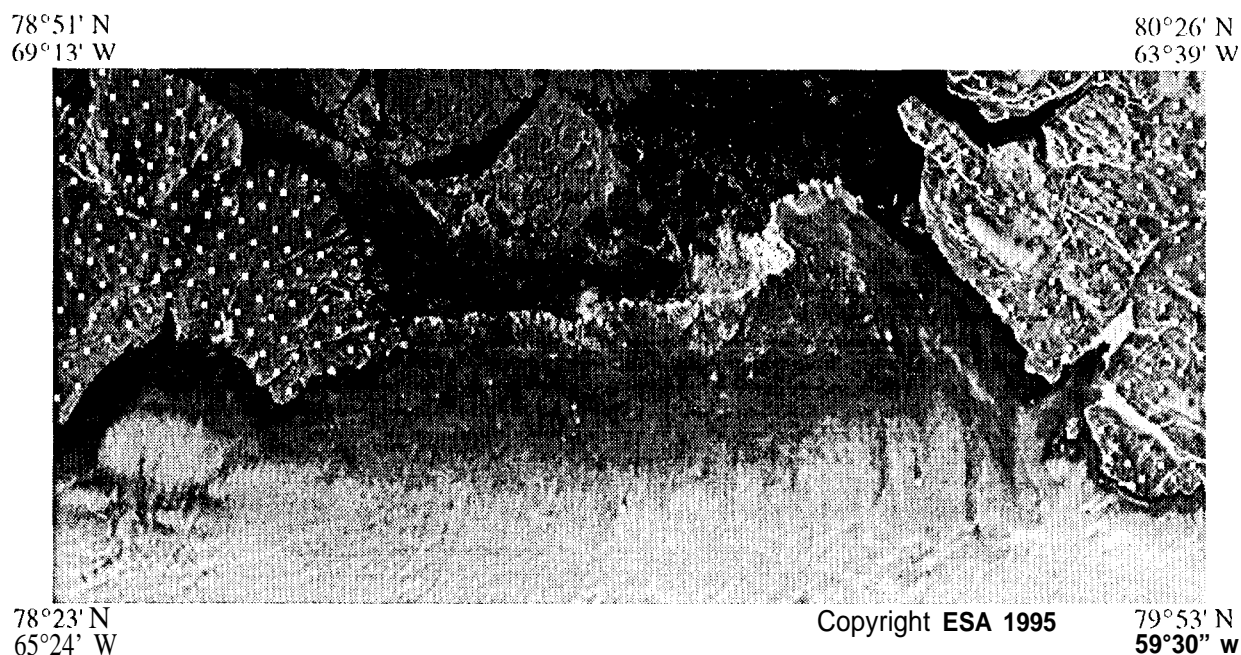


Figure 7. SAR amplitude image of the Humboldt Glacier, Greenland. The dimensions of the image are approximately 97 km across by 210 km long. The white squares indicate the locations of tie points used to estimate the baseline.

images. This did not eliminate the additional problem of streak errors (Rignot and others, 1994; Joughin and others, 1995b), which are not processor-induced artifacts. Streaks found in the data for this study are too small to have a significant effect on velocity error. Using the three images we formed two 3-day interferograms with the image from orbit 2947 common to both. The baseline for the 2904/2947 interferogram is approximately 236 m, and the baseline for the 2947/2990 interferogram is approximately -10 m.

To cancel the effect of motion, we differenced the interferograms to yield a topography-only interferogram with an effective baseline of -246 m (Joughin and others, 1995b). This interfero-

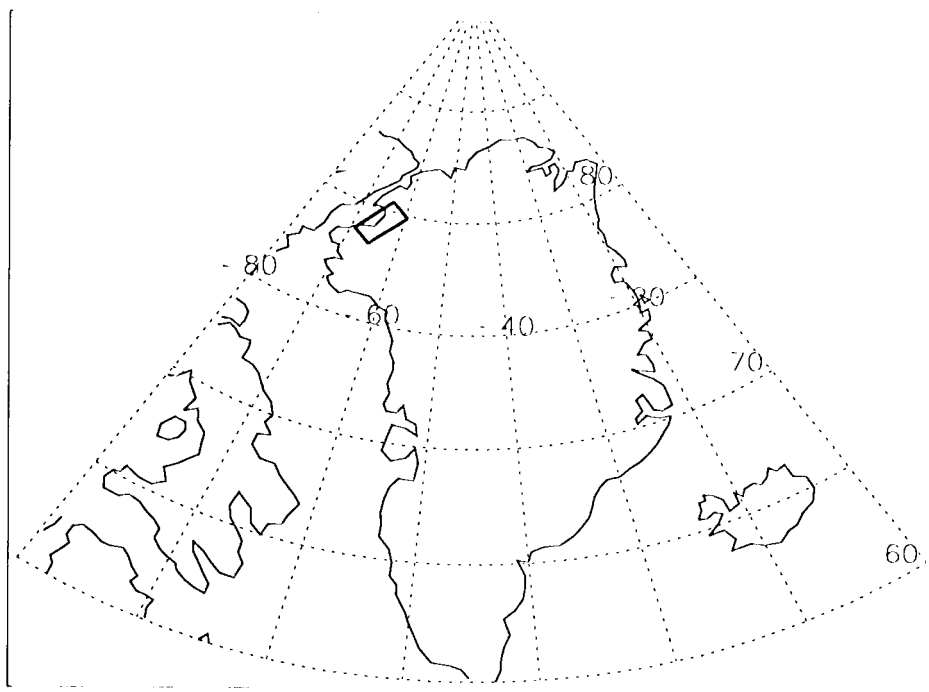


Figure 8. Map of Greenland showing the location of SAR image containing the terminus of the Humboldt Glacier.

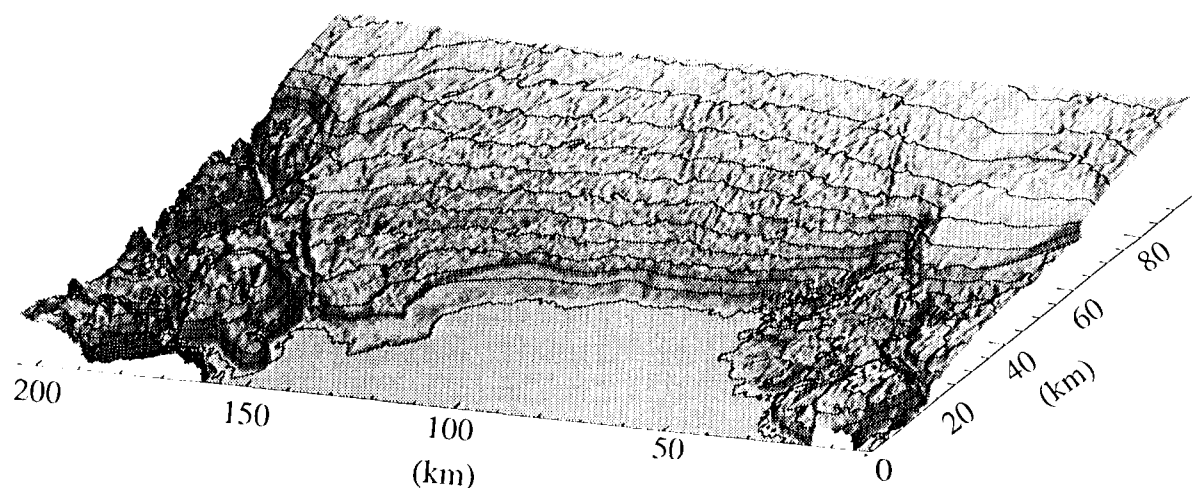


Figure 9. Interferometrically -derived DEM of the lower part of the Humboldt Glacier. Bed-rock elevations were determined photogrammetrically (Ekholm, Personal Communication). The contour interval is 100 m. Illumination is directed from overhead along the vertical axis.

gram was used to create a DEM for the area on the ice sheet. Figure 9 shows this DEM as a shaded surface overlaid with 100 m contours. In the bedrock areas phase gradients caused by steep slopes made it difficult to unwrap the phase. This problem could be eased by using a shorter baseline. We are primarily interested in the ice sheet, however, so we chose a longer baseline to achieve better accuracy and did not attempt to determine the bedrock topography. The bedrock elevations in Figure 9 are extracted from the same DEM that we used for tie-point information, which was provided by S. Ekholm (personal communication) of KMS (National Survey and Cadastre). There was too much decorrelation to unwrap the phase for a narrow band along the calving face. This part of the DEM has been filled in with elevation data from the KMS DEM. The lower resolution of the KMS data causes this area to appear smoother than adjacent regions in the shaded surface representation.

It is possible to interferometrically measure ice-sheet elevations with 4 m absolute and 2.5 m relative accuracy (Joughin and others, 1995b). DEM accuracy is largely determined by the quality of the tie points used to estimate the baseline. The Humboldt scene is near the coast, where altimetry-derived tie points on the ice sheet are the most in error because of high surface slopes. These tie-point errors may cause our DEM to have a systematic error in the form of an along- and across-track tilts that could yield errors of up to several 10's of meters. We hope to determine the accuracy of this DEM using laser altimeter data from the NASA Arctic ice mapping lidar when it becomes available. We will also be able to improve the accuracy of the DEM using laser-altimeter tie points for the baseline estimate. Our current need for the DEM is to compute surface slopes to estimate velocity using (24). Our DEM is well suited for this purpose since slope estimates are relatively unaffected by tie-point errors.

We used the 2947/2990 interferogram to estimate the across-track velocity field for the Humboldt. Tie points from areas of bedrock (indicated by white dots in Figure 7) were used to estimate the baseline parameters: $\hat{B}_n^c = -11.20$ m, $\hat{B}_p^c = 24.17$ m, $\delta\hat{B}_n = 17.17$ m, and $\delta\hat{B}_p = -7.40$ m. The baseline for this interferogram is much shorter than that of the topography-only interferogram, so regions consisting of bedrock were easily unwrapped. The effect of topography was removed using a synthetic interferogram created using the DEM. The result, $\phi_{displacement}$, is shown in Figure 10. The phase is displayed wrapped (i.e., modulo- 2π) with irrelevant areas (i.e., sea ice) and areas that could not be unwrapped masked out.

We need to know the component of velocity in the along-track direction, v_x , to estimate v_y using (24). We do not have an interferogram from a second look direction, so we have no direct knowledge of v_x . If we knew the flow direction, then we could determine v_x from v_{flow} .

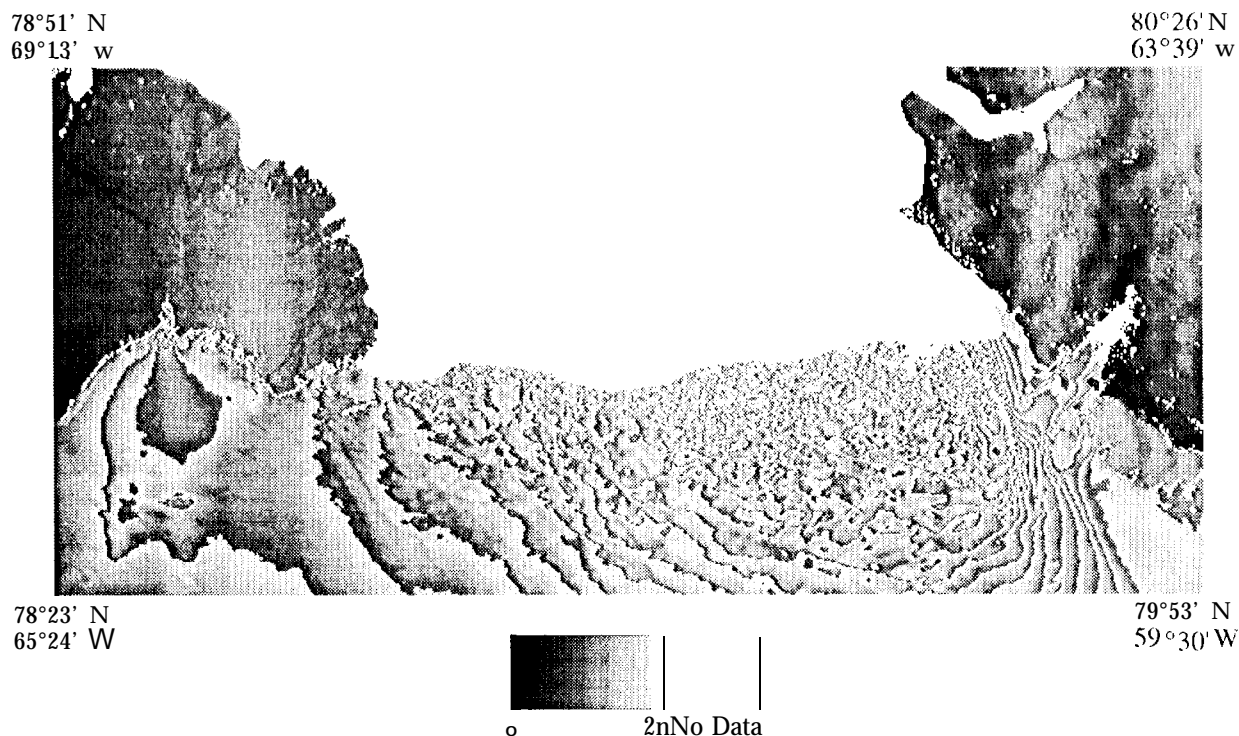


Figure 10. Interferometric phase, $\phi_{displacement}$, due to surface displacement in the radar look direction that occurred between February 7 and February 10, 1992. Areas with no data correspond to regions where the phase could not be unwrapped or was masked (i.e., to avoid regions with sea ice).

direction can be estimated from the direction of maximum averaged downhill slope (Paterson, 1994). This yields an averaged flow direction that misses perturbations in the direction of flow on scales less than a few ice thicknesses. Nevertheless, in the absence of other directional information this method may provide reasonable results.

In the Humboldt interferogram the across-track direction is nearly aligned with the direction of flow in most areas so that v_x is small with respect to v_y . Therefore we neglect v_x in our estimate of v_y . This is simpler and works almost as well as estimating flow direction from surface

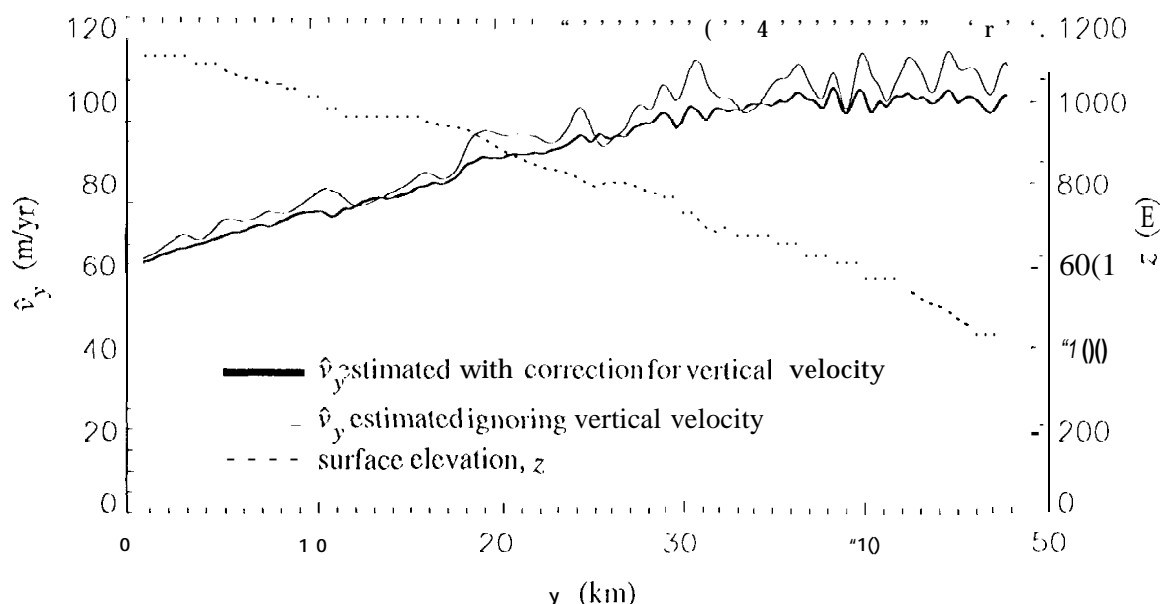


Figure 11. Examples of horizontal velocity estimates made with and without correction for vertical velocity. Surface elevation is also shown.

slopes. Since we are not estimating strain rates, the slightly larger error with this approach is insignificant.

Figure 11 shows estimates of v_y along a profile from the Humboldt data made, with and without correction for v_z . Comparison of the profiles indicates that ignoring v_z leads to erroneous short-scale variability in the estimate, \hat{v}_y , of up to 10 m/yr. This error is removed when the velocity is determined using (24). The correction is imperfect for this example because v_x is not known. Therefore, it is difficult to tell how much of the variability in the corrected profile is due to gradients in the horizontal velocity. This problem could be resolved with an interferogram from a second look direction.

Figure 12 shows the contours of the across-track velocity field for the Humboldt. At slightly

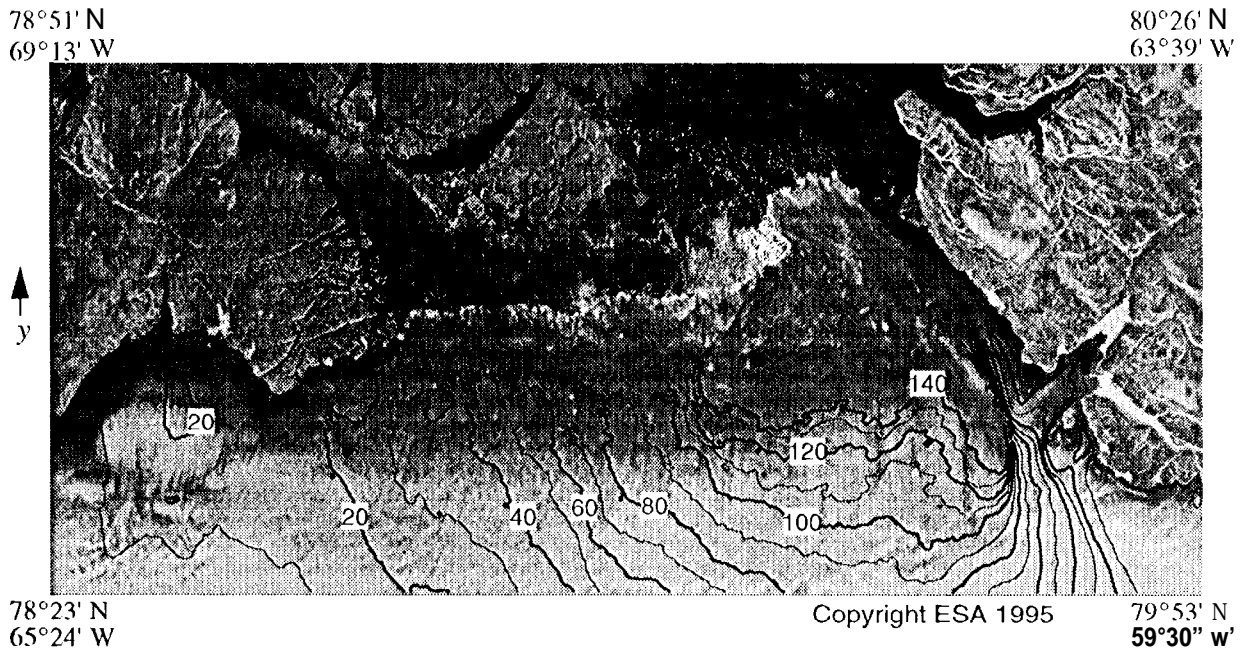


Figure 12. Contours of across-track velocity, v_y (m/yr), overlaid on SAR amplitude image.

more than 100 km, the Humboldt glacier has the widest calving face of any outlet glacier in the northern hemisphere. It appears from the SAR imagery (Figure 7) that most of the calving face is grounded, making this perhaps the longest continuous extent of grounded calving ice anywhere. Although the width of the Humboldt makes it the largest outlet glacier in Greenland, the velocity field for this glacier (Figure 7) reveals that the ice-flow speeds are not extreme, and also that the enhanced speeds do not reach great distances inland. With ice flow speeds of less than 100 m/yr only 15 km from the calving front over the southwestern half of the glacier, it is clear that most of the discharge flux is carried in the more rapidly flowing northeastern half. Flow in this area exceeds speeds of 140 m/yr 25 km from the calving face and produces a region of enhanced shear on the northeastern margin. This enhanced flow may be due to the presence of a channel in

the bedrock.

We do not have independent estimates of ice velocity to directly evaluate the accuracy of our results. On the areas of bedrock, the velocity is zero, so we can estimate error for bedrock regions. The mean of the residual phase error for the bedrock area is 0.37 radians, and the standard deviation is 1.54 radians. This is equivalent to a velocity error with a mean of 0.52 m/yr and a standard deviation of 2.1 m/yr.

In the previous section we estimated error due to baseline inaccuracy by means of simulation. To apply this procedure to the Humboldt area, we need to know the phase error and tie-point error. We do not have an accurate estimate of the error for tie points extracted from the KMS DEM. Instead, we use the standard deviation of the residual phase error for the ice free regions, which is affected by both conventional phase error and phase error due to uncompensated topography from error in the DEM. The contribution from DEM error serves as an estimate of the tie-point error, scaled to the equivalent level of phase error. Thus, when the residual phase error is used in the simulation, the effect of tie-point error does not have to be included explicitly as in the previous section. By doing this, we overestimate the combined effects of conventional phase error and tie-point error. This is because the residual phase error is also affected by error in the baseline estimate, σ_{e_B} . This is a relatively minor effect, however, as baseline error is smallest in the vicinity of the tie points.

The results of the simulation indicate that for the Humboldt scene, the maximum standard deviation of the velocity error due to baseline error is $\sigma_{e_B, v_y} = 0.99$ m/yr. Combining this error with the combined estimate of phase and DEM error from the ice-free areas (2.1 m/yr), the maximum velocity error on the ice-covered area is 2.3 m/yr. Actual errors may be slightly larger due

to uncompensated vertical motion since v_x was ignored in applying (24).

in the prior simulations we assumed a low value ($\sigma_\phi = \frac{\pi}{20}$ radians) for the phase noise. Even if large DEM errors are assumed, the portion of the 1.54 radian residual error attributable to conventional phase noise from speckle is larger than expected (i.e., $\sigma_\phi > 1$ radian). In particular, the phase of the bedrock area in the upper right corner of Figure 10 has a mottled appearance, which indicates an unanticipated source of phase error. Unlike conventional phase noise, which varies independently from pixel to pixel, this error has spatial structure over length scales of several kilometers. The baseline for this part of the image is too short to attribute this phase variation to uncompensated topography. Baseline errors would yield more regular tilt errors. Phase error with similar structure has been observed by Goldstein (1995) for an area in the Mojave desert. He attributed its cause to additional time (phase) delay due to turbulent water vapor in the lower atmosphere. It is possible that the features in our data are the result of a similar phenomenon. It is interesting to note that the greatest anomalous phase variations are associated with areas containing the most rugged topography. Further research is needed to resolve the exact cause and effect of these phase anomalies. Whatever their cause, these features raise the level of phase error. Furthermore, because the error is spatially correlated it cannot be reduced by simple filtering, as is the case for phase noise due to speckle.

CONCLUSIONS

The results of the simulations suggest some rules that should be applied when choosing tie points. Four GPS-measured velocity tie points can provide good accuracy over large inland areas. The best way to improve accuracy with only 4 points is to maximize the spacing between

points. To reduce error caused by errors in locating tic points within SAR imagery, areas with low strain rates are preferable. Tic points can be automatically geolocated within SAR imagery so that tic points need not be associated with any radar-visible features.

For coastal areas, a reasonably detailed map (i.e., horizontal resolution of a half kilometer or better) and a sufficient area of exposed bedrock allow the baseline estimate to be extended onto the ice sheet with acceptable accuracy. The ability to use many tic points means that high accuracy is possible even with tic-point elevation errors on the order of 100 m for areas within 100-200 km of the coast. If large areas of bedrock are available, it is possible to extend the velocity estimates much further inland with reasonable accuracy.

Our results have demonstrated that ice velocities accurate to within a few meters per year can be determined with satellite radar interferometry, although accuracy varies greatly with the quality of tic points. If both ascending and descending images are acquired during the tandem phase of ERS 1/2, then it will be possible to map the full three-dimensional velocity field assuming surface parallel flow. The detailed velocity and topography information rendered by satellite radar interferometry provides an important new source of data for ice-sheet study.

ACKNOWLEDGEMENTS

1, Joughin and R. Kwok performed this work at the Jet Propulsion Laboratory, California Institute of Technology under contract with NASA. Mark Fahnestock was supported under NMTPE grant 5121 -J'P-O] 29.

We thank S. Ekholm of the National Survey and Cadastre, Copenhagen, Denmark for providing us with the DEM.

REFERENCES

- Likholm S. 1994. Personal communication, National Survey and Cadastre, 1 Denmark.
- Fahnestock M., R. Bindenschadler, R. Kwok, and K. Jezek. 1993. "Greenland ice sheet surface properties and ice dynamics from M-W-1 SAR imagery," *Science*, vol. **262**, pp. **1530-1534**.
- Ferrigno J. G., B. K. Lucchitta, K. F. Mullins, A. L. Allison, R. J. Allen, and W. G. Gould. 1993. "Velocity measurement and changes in position of Thwaites Glacier/iceberg tongue from aerial photography, Landsat images and NOAA AVHRR data," *Annals Of Glaciology*, vol. **17**, pp. 239-244.
- Gabriel, A. K., R. M. Goldstein, and H. A. Zebker. 1991. "Mapping small elevation changes over large areas: differential radar interferometry," *Journal of Geophysical Research*, vol. **94**, no. B7, pp. 9183-9191.
- Goldstein R. M. 1995. "Atmospheric limitations to repeat-track radar interferometry," *Geophysical Research Letters*, vol. **22**, no. 18, pp. 2517-2520.
- Goldstein R. M., H. Engelhardt, B. Kamb, and R. M. Frolich. 1993. "Satellite radar interferometry for monitoring ice sheet motion: application to an Antarctic ice stream," *Science*, vol. **262**, pp. 1525-1530.
- Goldstein, R. M., H. A. Zebker, and C. L. Werner. 1988. "Satellite radar interferometry: two-dimensional phase unwrapping," *Radio Science*, vol. **23**, no. 4, pp. 713-720.
- Jezek K., and F. Rignot. 1994. "Katabatic wind processes on the Greenland ice sheet," presented at the *AGU Fall Meeting*, San Francisco.
- Joughin, I. R., D. F. Winebrenner, and M. A. Fahnestock. 1995a, "observations of ice-sheet motion in Greenland using satellite radar interferometry," *Geophysical Research Letters*, vol. **22**, no. 5, pp. 571-574.
- Joughin, I., D. Winebrenner, M. Fahnestock, R. Kwok, W. Krabill, 1995b, "Measurement of ice-sheet topography using satellite radar interferometry," *Journal of Glaciology*, in press.
- Joughin, I. R. 1995. *estimation of Ice Sheet Topography and Motion Using Interferometric Synthetic Aperture Radar*, Ph. D. Thesis, University of Washington.
- Kwok R., M. A. Fahnestock. 1996. "Ice sheet motion and topography from radar interferometry," *IEEE Trans. Geosci. Rem. Sen.*, vol. **34**, no. **1**.
- Li, F. K., and R. M. Goldstein. 1990. "Studies of multi-baseline spaceborne interferometric synthetic aperture radars," *IEEE Trans. Geosci. Rem. Sen.*, vol. **28**, no. 1, pp. 88-97.

Massonnet D., M. Rossi, C. Carmona, F. Adragna, G. Peltzer, K. Feigl, and J. Rabaute. 1993. "The displacement field of the Landers earthquake mapped by radar interferometry," *Nature*, vol. 364, no. 6433, pp. 138-142.

Paterson, W. S. B. 1994. *The Physics of Glaciers*. 3rd ed. Oxford: Pergamon Press,

Press, W. H., Teukolsky, S. A., Vetterling, W. T., and Flannery, B. P. 1992. *Numerical Recipes in C, the Art of Scientific Computing*. 2nd ed. Cambridge: Cambridge University Press.

Rignot, F., K. C. Jezek, and H. G. Sohn. 1995. "Ice flow dynamics of the Greenland ice sheet from SAR interferometry," *Geophysical Research Letters*, vol. 22, no. 5, pp. 575-578.

Rodriguez, F., and J. M. Marlin. 1992. "Theory and design of interferometric synthetic aperture radars," *IEEE Proc.-F*, vol. 139, no. 2, pp. 147-159.

Scambos, T. A., M. J. Dutkiewicz, J. C. Wilson, and R. A. Bindshadler, 1992. "Application of image cross-correlation to the measurement of glacier velocity using satellite image data," *Remote Sensing of the Environment*, vol. 42, pp. 177-186.

Solaas G. A. 1994. "1 IRS-1 SAR interferometric baseline algorithm verification," version 1.1. no. ES-TN-DPI-OM-GS02, ESA/ESRIN, Frascati, Italy.

Zebker, H. A., C. L. Werner, P. A. Rosen, and S. Hensley. 1994. "Accuracy of topographic maps derived from IRS-1 interferometric radar," *IEEE Trans. Geosci. Rem. Sen.*, vol. 32, no. 4, pp. 823-836.

Zebker, H. A., S. N. Madsen, J. Martin, K. B. Wheeler, T. Miller, Y. Lou, G. Alberti, S. Vetralla, and A. Cucci. 1992. "The TOPSAR interferometric radar topographic mapping instrument," *IEEE Trans. Geosci. Rem. Sen.*, vol. 30, no. 5, pp. 933-940.